

Cosmic Web: Origin and Observables

Dmitry Pogosyan¹, J. Richard Bond¹, Lev Kofman¹ and James Wadsley^{1,2}

¹ *Canadian Institute for Theoretical Astrophysics, University of Toronto,
60 St. George St., Toronto, ON M5S 3H8, Canada*

² *Astronomy Department, Univ. of Washington, Box 351580, Seattle WA 98195-1580*

Abstract. Simple analytic arguments are used to understand the predominantly filamentary web in the large-scale distribution of galaxies. Numerical simulations of superclusters are performed to assess the feasibility of directly mapping the intracluster webbing, in particular with weak gravitational lensing using Wide Field Cameras.

1 Patterns in random density fields

In [1] we have shown (see also [2] in this volume) that the large-scale structure in N-body simulations, which is believed to describe adequately the galaxy distribution in redshift catalogues, can be explained directly by the geometry of the initial density field, amplified by gravitational instability. While rich clusters of galaxies form from high density enhancements of scales $R_f \sim 8 \text{ h}^{-1} \text{ Mpc}$, intracluster filamentary webbing reflects initial connections in the random density field bridging these protocluster regions at lower density thresholds.

The quantitative study of the properties of 3D random fields in a cosmological context goes back to the famous formula of Doroshkevich [3] for the joint distribution function $P(\lambda_1, \lambda_2, \lambda_3)$ of the ordered eigenvalues $\lambda_1 \leq \lambda_2 \leq \lambda_3$ of the initial deformation (shear) tensor e_{ij} . The latter is related to the density field, given in Fourier space by (random) amplitudes $\delta(\mathbf{k})$, by

$$e_{ij}(\mathbf{r}) = - \int \frac{d^3 \mathbf{k}}{(2\pi)^3} \hat{k}_i \hat{k}_j \delta(\mathbf{k}) W(kR_f) e^{i\mathbf{k} \cdot \mathbf{r}}. \quad (1)$$

The filter $W(kR_f)$ separates the smooth large-scale field which evolves in the mildly nonlinear single-stream regime from the highly nonlinear short-scale chaotic flow.

Usually, the dynamical role of the shear in a local gravitational collapse is being focused on. Here we stress another aspect of the shear tensor: as a shape parameter describing the *geometry* of the initial density field. The mean overdensity profile around a field point \mathbf{r}_0 with known values of the shear, $\langle \delta(\mathbf{r}) | \lambda_1(\mathbf{r}_0), \lambda_2(\mathbf{r}_0), \lambda_3(\mathbf{r}_0) \rangle$, where $\delta = \rho/\bar{\rho} - 1$, as illustrated in Fig. 1, shows that the shape depends on the sign of the shear eigenvalues (see [4] for details of these and subsequent analytical calculations, also [5]). In effect, the local shear signature defines the curvature of the density isocontours up to a distance of

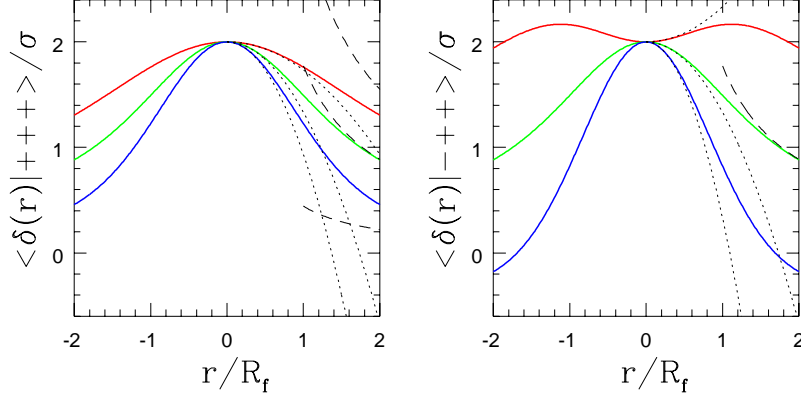


Figure 1: Constrained primordial density field $\langle \delta(\mathbf{r}) | \lambda_1, \lambda_2, \lambda_3 \rangle$ as a function of distance \mathbf{r} in units of the filter scale R_f , in the three eigendirections (1-top, 3-bottom). The left plot corresponds to the shear with all positive (+++) eigenvalues. The right plot represents the case of "filamentary" behaviour of the density in the neighbourhood of the (-++) sheared point. Dotted and dashed curves show the analytic short and long distance asymptotics [4].

several R_f .¹ The increase in the density along one axis while falling off along the remaining two is symptomatic of filamentary bridges that connect the higher density regions where the shape of the density profile is more spherical. Fig. 2 shows that local properties of the shear tensor determine whether the region is part of the filamentary or protocluster structure.

This correspondence between the global properties of the density field and local characteristics of the shear tensor enables analytical estimation of the gross properties of the Cosmic Web. For instance, the probability of the eigenvalue signature given the density threshold δ , $P(\text{sign}|\delta)$, shows which structures dominates depends on the isodensity threshold chosen. Fig. 3 shows that at overdensities above a critical δ , 1.56σ for Gaussian fields, one encounters predominantly spherical-like mass concentrations, while at the lower density contrast, $0 < \delta < 1.56\sigma$, most of the initial density enhancements are in elongated filamentary bridges. Planar configurations (---) are less likely for any positive overdensities $\delta > 0$. The related quantity $P(\delta|\text{sign})$ gives us the density distribution within different types of structure. While the average density of the filaments in the initial configuration is equal to 0.6σ (Fig. 3), it is the $1.5\text{--}2\sigma$ excursions which are precursors of the rare prominent filaments. In contrast, even rare planar, membrane-like, configurations are expected only at lower overdensities of $0.5\text{--}1\sigma$.

¹The information contained in the density curvature tensor $\delta_{,ij}$ itself is much more local and less representative of the density behaviour at large distances from the constraint point.

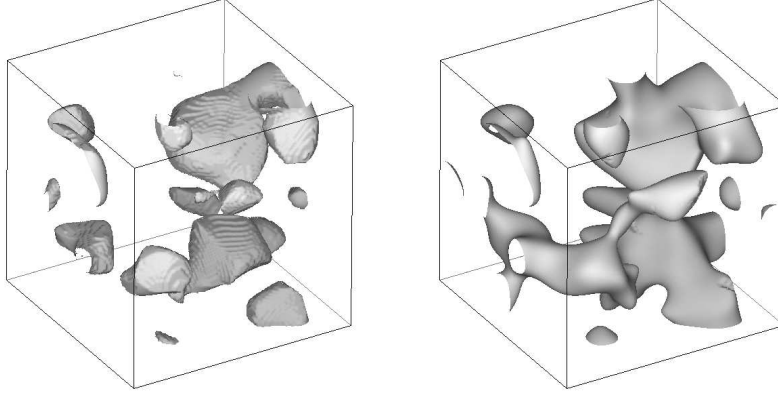


Figure 2: Example of the cosmological initial density field. Left panel: the part of space with overdensity $\delta \geq 1\sigma$ and $\lambda_3 \geq \lambda_2 \geq \lambda_1 > 0$. Note the roughly spherical shapes of the regions drawn. Right panel: the overdense regions with $\delta \geq 1\sigma$ and $\lambda_3 \geq \lambda_2 > 0$ but arbitrary λ_1 . Inclusion of the points with $\lambda_1 < 0$ creates filamentary connectors between round $\lambda_1 > 0$ regions.

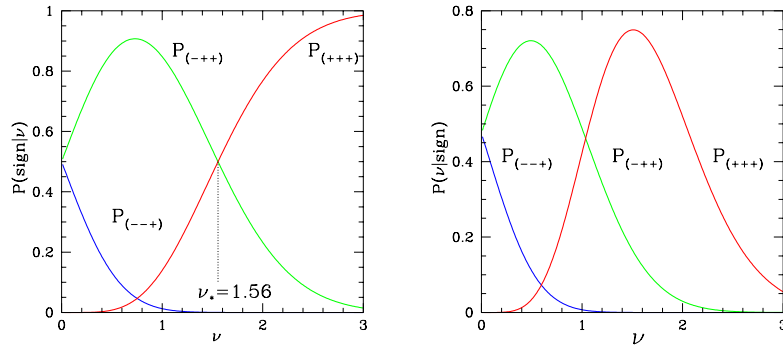


Figure 3: Left panel: Probability of the eigenvalue signature given the overdensity threshold $P(\text{sign}|\nu)$, $\nu = \delta/\sigma$. Right panel: Density distribution given the type of shear tensor, $P(\nu|\text{sign})$. Mean densities for the given shear type are $\bar{\delta}_d \approx 1.66\sigma, 0.6\sigma, -0.6\sigma$ for $(+++), (-++)$ and $(--+)$ cases labeled by $d = 3, 2, 1$ with dispersion $\sigma_d \approx 0.55\sigma$ almost equal for all configurations.

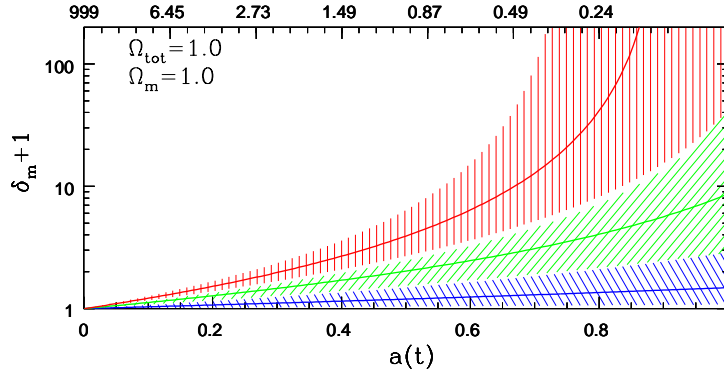


Figure 4: The nonlinear density evolution $\delta(t)$ of idealized spheres (top curve), filaments (middle) and membranes (bottom) of Lagrangian scale R_f for which the smoothed linear *rms* amplitude of density fluctuations $\sigma(R_f)$ is 0.65. Solid curves show $\delta(t)$ for the structures with initial (linear) density equal to $\bar{\delta}_d + 2\sigma_d$, $d = 1, 2, 3$. The shaded bands delineate the range of $\delta(t)$ for initial densities $[\bar{\delta}_d + \sigma_d, \bar{\delta}_d + 2.5\sigma_d]$. Values of $\bar{\delta}_d$ and σ_d are given in Fig. 3.

As a simple nonlinear model for evolution of clusters, filaments and membranes, let us consider the evolution of a shell which is spherical ($d=3$) or cylindrical ($d=2$) of radius $R(t)$, or planar ($d=1$) of width $2R(t)$ which expands with the Hubble flow in the other $3 - d$ directions (c.f. Fillmore and Goldreich [6]). The shell is characterized by its Lagrangian tophat scale R_f and the linear overdensity within the shell δ_d . Evolution of the shell radius in different cosmologies with scale factor $a(t)$ is given by ²

$$\ddot{R} = H_0^2 \left[\frac{(3-d)}{2d} \Omega_m + a^3 \Omega_\Lambda - \frac{3\Omega_m}{2d} (1 + D(t_i)\delta_d) \left(\frac{aR_f}{R} \right)^d \right] \frac{R}{a^3}. \quad (2)$$

As we have shown, for cosmological initial conditions typical linear overdensities δ_d at the same scale R_f are quite distinct for structures of different geometry. Solving Eq.(2) with δ_d suggested by Fig. 3 demonstrates the range of present time densities one can expect for objects of different shape on the basis of this elementary theory. Results are presented in Fig. 4. For filaments we have $\rho \approx 3-12 \bar{\rho}$. Although filamentary structures have, generally, turned around, only rare filaments are approaching collapse by the present time. Membranes, which are still expanding, have $\rho \approx 1-3 \bar{\rho}$. These values should be compared with the density of the collapsed spherical halos at the moment of virialization, $\approx 180 \bar{\rho}$. N-body simulations confirm these simple estimates.

² Ω_m and Ω_Λ are present-day density parameters of the matter and the cosmological constant. $D(t_i)$ is the growing mode at the onset of integration, $\dot{R}(t_i) = \dot{a}(t_i) [1 - D(t_i)\delta_d/d] R_f$

2 Observability of the Cosmic Web

The filamentary pattern that joins galaxy clusters into a complex web is manifest in 3D galaxy catalogues. However the question of biasing between the galaxy distribution and the underlying mass density remains open. In recent work [7] we evaluated the feasibility of mapping the intracluster structure using observational techniques directly probing large-scale dark matter and gas distributions. We have performed gasdynamical simulations (using a SPH+TreeP³M code [8]) of several rich supercluster regions and considered the weak gravitational lensing of high redshift galaxies by the low redshift structure, the secondary variations in CMB temperature induced by the Sunyaev-Zeldovich effect and the X-ray emission by hot gas in clusters and along the filaments. The simulations and SZ maps derived from them are described in our companion paper [2].

Since the lensing depends upon the projected density Σ , not pressure as for the SZ effect or density-squared as for the X-rays, weak lensing would be a better probe for the filaments if the signal-to-noise is large enough. There are two sources of noise, one the intrinsic (random) ellipticities of the source galaxies, and the other shear from ambient large scale structures along the line-of-sight confusing the ellipticity pattern created by the filamentary web.

Results of our simulations for standard CDM, open CDM and a CDM model with a cosmological constant are presented in Fig. 5. They demonstrate that cluster-cluster bridges at redshifts $z \sim 0.5$ are sufficiently developed to produce lensing of background galaxies at the level of several percent which can be detected in the images of modern wide field cameras. One such detection of the bridge between two close clusters in the field of three at $z = 0.4$ is described in [9].

Acknowledgements. D.P wishes to thank the organizers of the XIV IAP Colloquium for financial support.

References

- [1] Bond, J.R., Kofman, L. & Pogosyan, D., 1996, *Nature* 380, 603.
- [2] Bond, J.R., Kofman, L., Pogosyan, D. & Wadsley, J.W., 1998, this volume.
- [3] Doroshkevich, A., 1970, *Astrofizika* 6, 581.
- [4] Bond, J.R., Kofman, L. & Pogosyan, D., 1997, preprint CITA
- [5] Bardeen, J.M., Bond, J.R., Kaiser, N. & Szalay, A.S. 1986, *ApJ* 304, 15
- [6] Fillmore, J. & Goldreich, P., 1984, *ApJ* 281, 1.
- [7] Bond, J.R., Kofman, L., Pogosyan, D. & Wadsley, J.W., 1998, *in preparation*.
- [8] Bond, J.R. & Wadsley, J.W., 1997, eds Petitjean P. & Charlot S., in *Proceedings of the XIII IAP Colloquium*, Editions Frontieres, Paris, p. 143
- [9] Kaiser, N., *et al.* , 1998, submitted to *ApJ*

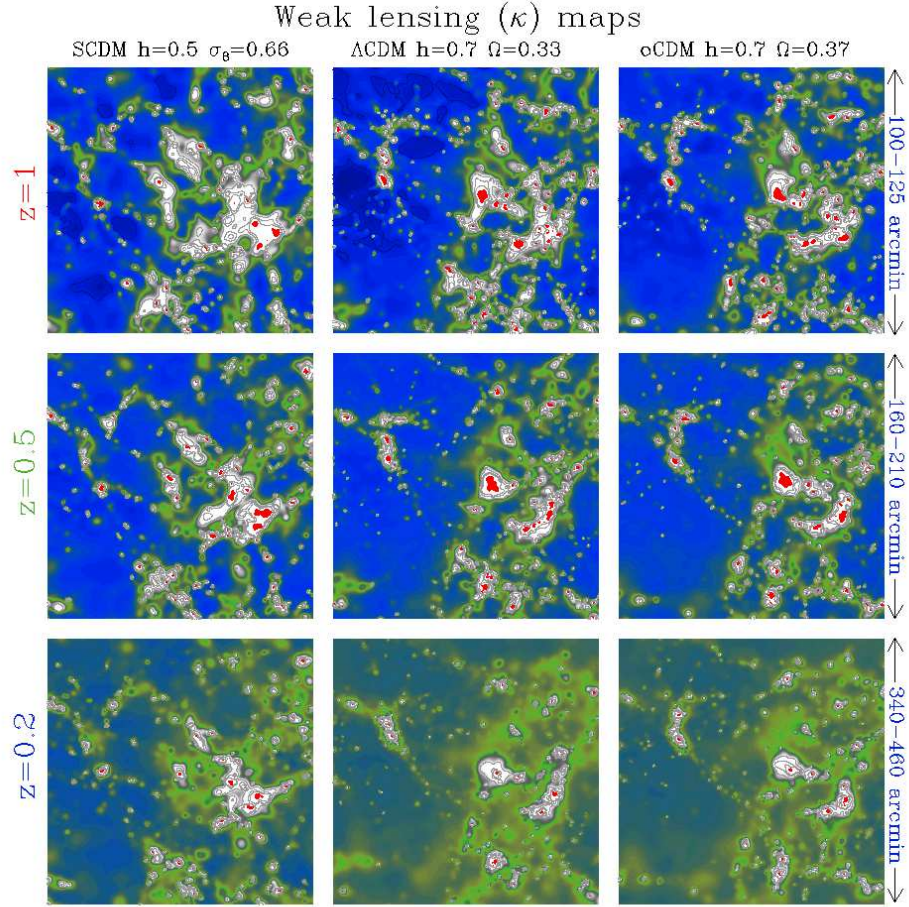


Figure 5: Colour maps of the convergence $\kappa = -2\Sigma/\Sigma_{\text{crit}}$ for our compact supercluster simulations at $z = 0.2, 0.5$ and 1 . Σ is the surface density (with the mean taken out), and the critical density Σ_{crit} depends upon the comoving distance to the lens and the source. We assumed the latter are at redshift $z = 2$ for these plots. White areas correspond to $\kappa < -0.04$ with grey contours marking the levels $-0.08, -0.12, -0.16$. Red dots denote high density regions $\kappa < -0.3$. The level of convergence in the green areas is ~ -0.02 . See Figs. 4,5 of [2] for the corresponding dark matter distributions and SZ maps.